Insight into the Fergusonite−Scheelite Phase Transition of ABO_4-Type Oxides by Density Functional Theory: A Case Study of the Subtleties of the Ground State of $BiVO_4$

Taifeng Liu,* Xingfan Zhang, Jingcheng Guan, C. Richard A. Catlow, Aron Walsh, Alexey A. Sokol,* and John Buckeridge*

ABSTRACT: $BiVO_4$ (BVO) is an important photocatalytic and ferroelastic material. It has been extensively studied using density functional theory (DFT). However, on optimization, at a commonly employed level of theory using the Perdew−Burke−Ernzerhof (PBE) exchange−correlation functional, the monoclinic scheelite (*ms*-BVO) structure transforms into a higher-symmetry tetragonal scheelite (*ts*-BVO) phase spontaneously, which has also been confirmed by other groups. Such a transformation is highly unusual, as one would expect the transition to a lower symmetry structure to be modeled well at this level of theory, as is the case with, for example, the perovskite $BaTiO_3$, and hints at a subtle interplay between structural and electronic properties. In this work, we demonstrate that this phase transition nevertheless can be described accurately with DFT but only using a hybrid density functional with ∼60% Hartree−Fock (HF) exchange. We find a soft phonon mode in *ts*-BVO, which corresponds to the phase transition from *ts*-BVO to *ms*-BVO associated with a double-well potential characterizing this phase transition, implying that the transition is of the second order. We find two key factors that can explain thissurprising behavior. First, the polarizability of the Bi^{3+} ion, with an on-site contribution from the hybridization of its 6s and 6p states,is notably underestimated by DFT. Moreover, the effective radius of the Bi^{3+} ion proves to be too large. With the 60% HF exchange hybrid functional, the description of the polarizability of Bi^{3+} does not improve but the radii of the Bi^{3+} ions approach more realistic values. The polarizability of the O and V ions are reasonably described already by PBE. To gain further insight into the problem, we investigated the structural stability of other ABO_4 oxides, including $ScVO_4$, $LaNbO_4$, $YTaO_4$, and $CaWO_4$, and related materials. Some of them have similar behavior to BVO, whose ground-state monoclinic structure proves to be unstable using commonly employed DFT approaches. In particular, for $ScVO_4$, we found that the scheelite tetragonal and fergusonite monoclinic structures cannot be distinguished using the PBEsol functional. But the fergusonite monoclinic structure becomes stable using the hybrid functionals with high fractions of HF exchange, which points to the crucial role of the accurate ionic size reproduction by the methodof choice as the on-site Sc^{3+} polarizability is too low to have a significant effect. Our findings would be of high interest for the study of other problematic materials with subtle size and polarization properties, especially ABO_4 oxides that undergo similar phase transitions.

1. INTRODUCTION

$BiVO_4$ (BVO) has attracted much attention in recent years in photocatalysis and photoelectrochemical water splitting due to its visible light activity, favorable conduction and valence band edge positions, and low-cost facile synthesis route.[1−6] Moreover, it is an important ferroelastic material.[7] The phase transition between the low-temperature ferroelastic monoclinic scheelite (*ms*-BVO) and the high-temperature paraelastic tetragonal scheelite (*ts*-BVO) is also widely investigated.[8−11]

Both phases have a crystallographic unit cell of four formula units. At ∼528 K, the material undergoes a reversible second-order phase transition from *ms*-BVO (space group $I2/a$) to *ts*-BVO (space group $I4_1/a$), in which the primitive unit cell of two formula units transforms as shown in Figure 1[12] This transition is driven by the $q \sim 0$ soft optical phonon B_g mode.[13]

BVO is not unique and there are still many other ABO_4 materials having a similar phase transition.[15] The ABO_4 type ortho-niobates are generally observed to adopt the monoclinic (space group $I2/a$) fergusonite-type structure, and the term "fergusonite" is loosely used to describe the monoclinic ABO_4 oxides.[16] In particular, rare-earth niobates ($LnNbO_4$, Ln = La−Lu) are known to undergo a reversible, pure ferroelastic phase transition from a high-temperature paraelastic, scheelite-type (tetragonal, $I4_1/a$) to a ferroelastic, fergusonite-type (mono-

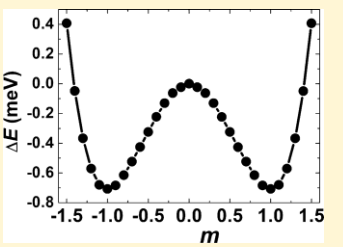
0.4
0.2
0.0
-0.2
-0.4
-0.6
-0.8
ΔE (meV)
-1.5 -1.0 -0.5 0.0 0.5 1.0 1.5
m

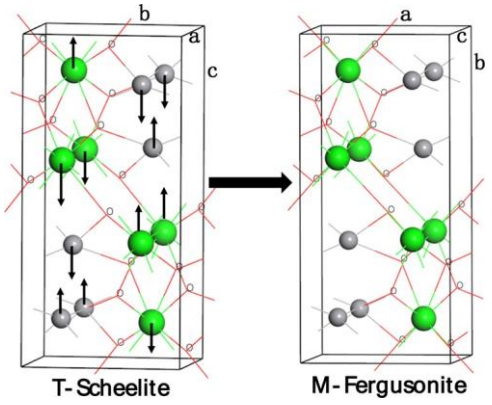

Figure 1. Tetragonal scheelite (T-Scheelite) and monoclinic fergusonite (M-Fergusonite) structures of ABO_4 oxide. Green spheres represent A atoms, gray spheres represent B atoms, and symbol "O" represents O atoms.[14] The displacements along the $T(B_g)$ mode for the phase transition in scheelite are shown with arrows.

clinic, $I2/a$) structure at low temperatures.[17−23] Moreover, it has been also established that in many other chemical classes of compounds of the ABO_4-type family (vanadates,[22,24−26] tantalates,[27] tungstates,[14] molybdates,[14] etc.) temperature or pressure induces structural transformation from the tetragonal scheelite-to-monoclinic fergusonite symmetry which is illustrated in Figure 1. The lattice constants of conventional scheelite and fergusonite structures are typically almost the same, as can be seen in the lattice constants of BVO analyzed below. A search in the Inorganic Crystal Structure Database (ICSD)[28] produces many large numbers of scheelite and fergusonite structured materials of diverse chemical compositions listed in Table 1.

Table 1. ABO_4 Vanadate, Niobate, Tantalate, Tungstate, and Molybdates Compounds with Scheelite and Fergusonite Structures

ABO_4 oxides	scheelite (A ions)	fergusonite (A ions)
AVO_4	Sc, Y, Sm, Eu, Ho−Lu	Sc, Sm, Eu, Ho, Lu
$ANbO_4$	Y, La−Nd, Sm−Lu	Y, La−Nd, Sm−Lu
$ATaO_4$	Y, Nd, Sm−Er	Y, Nd, Sm−Er
AWO_4	Ca, Sr, Ba, Pb, Eu	Ca, Sr, Ba
$AMoO_4$	Ca, Sr, Ba, Cd, Pb, Eu	Ca, Sr, Ba

Energy differences between the phases related to such structural transformations are usually very small which poses a serious challenge to computational studies. A uniformly accurate reproduction of the relevant parts of the energy landscape is in such cases an important prerequisite, and commonly, density functional theory (DFT) has been considered as a reliable method that should guarantee the necessary level of accuracy and is widely applied in materials physics, providing detailed insight into the properties of materials at the atomic level. And, indeed, DFT using semi-local functionals like Perdew−Burke−Ernzerhof (PBE),[29] or hybrid functionals that admix a low fraction (generally within the 20−25% range) of the nonlocal Hartree−Fock (HF) exchange, can reproduce or accurately predict experimentally observed phase transitions in many materials, including textbook perovskite structured $BaTiO_3$ and $SrTiO_3$.[30−34] Some of the scheelite-structured materials listed in Table 1 have already been investigated using DFT. Mullens et al.[35] found that the PBEsol functional works very well for both $SmNbO_4$ and $SmTaO_4$, but a greater discrepancy between the observed and calculated volumes was seen for the latter. The calculated and observed structural properties for $HoNbO_4$ were reproduced best using the PBEsol functional,[36] whereas the PBE functional-based calculations provided a better agreement with the experiment for both polymorphs (space group $I2/a$ and $P2/c$) of $HoTaO_4$.[35] The authors concluded there is no unique universal exchange−correlation functional appropriate for these types of oxides. Kuwabara et. al.[37] calculated the lattice constants of tetragonal (t-$LaNbO_4$, $I4_1/a$) and monoclinic (m-$LaNbO_4$, $I2/c$) using local density approximation (LDA) and generalized gradient approximation (GGA) PBE functional. They found that the monoclinic phase is more stable than the tetragonal one with LDA. In contrast, the t-$LaNbO_4$ has lower energy than m-$LaNbO_4$ in the GGA PBE functional calculation. Feng et. al.[27] studied the high-temperature phase transition between the tetragonal (schee- lite) and monoclinic (fergusonite) forms of $YTaO_4$ using a combination of first-principles calculations and a Landau free-energy expansion, and they found that the GGA PBE functional works well in this case.

Considering the case of BVO, we found, surprisingly, that both the popular GGA and hybrid level DFT with a low fraction of HF are unable to simulate the phase transition from ms-BVO to ts-BVO. When optimizing the lattice parameters and atomic positions of ms-BVO with either of the commonly employed DFT approaches, the monoclinic structure spontaneously transforms into the ts-BVO phase. In this paper, we demonstrate that the phase transition from ms-BVO to ts-BVO can only be reproduced or predicted accurately with a hybrid functional including a large fraction (∼60%) of HF and using unusually stringent convergence criteria.[38] We show that such an approach is essential to model the ground-state structure and the high-temperature phase transition accurately. This observation may have direct relevance to the investigation of phase transitions in other materials of the scheelite group, but as already can be seen from the recent work on the niobates and tantalates mentioned above, the method of choice can prove to be specific to each compound. What we can, however, conclude is that the scheelite structure has a unique feature in its sensitivity to the level of accuracy provided by the methodological approach.

Taking into account the computational cost, it is not feasible for us to investigate the whole class of these materials using hybrid functionals under the high convergence criteria, especially some of the rare-earth elements containing f electrons and having complex magnetic states. Here, we report a detailed study of the BVO, which is the main topic of our paper, but we also have scrutinized some of the representative scheelite-structured materials using the PBEsol functional focusing on the relative stability (and existence) of the scheelite and fergusonite structures. Furthermore, we have taken $ScVO_4$ as an example and performed more detailed calculations with hybrid functionals. The paper is organized into following sections: we give the computational details in Section 2, present and discuss the results in Section 3, and final conclusions are drawn in Section 4.

2. METHODS SECTION←COMPUTATIONAL DETAILS

We carried out DFT calculations using the Vienna Ab initio Simulation Package (VASP) code.[39,40] For the material without magnetic moment, such as BVO, we performed non-spin-polarized

calculations, but for the materials with magnetic moments, the spin-polarized method is used (predictably, running spin-polarized calculations on the BVO structures did not result in any spontaneous spin polarization). For the exchange and correlation term, Perdew−Burke−Ernzerhof (PBE),[29] PBE revised for solids (PBEsol[36]), and PBE0[41] hybrid functionals were used. We treat the O ($2s^2$, $2p^4$), V ($3p^6$, $4s^2$, $3d^3$), and Bi ($5d^{10}$, $6s^26p^3$) electrons as valence electrons, with the core electrons represented by the projector-augmented-wave (PAW) potential. The fraction of exact exchange interaction α in the hybrid functional was varied from 0.25 to 0.7 to identify a suitable α value. The electronic wave functions were expanded in a large plane wave basis set with an energy cut-off of 950 eV. Self-consistent DFT energies were converged to 10^{-8} eV per primitive cell, and geometry optimizations were deemed converged when the residual forces on the atoms were smaller than 4×10^{-4} eV/ Å. For the 12-atom primitive cell, A 6 × 6 × 6 *k*-point mesh across the first Brillouin zone was used.

To verify our findings for the *ms*-BVO structure from the plane wave PAW calculations with VASP, full potential all-electron calculations using atomic numerical basis functions were performed employing the PBEsol functional as implemented in the Fritz Haber Institute ab initio molecular simulations (FHI-aims) code.[42] The details of the input files including the basis set and relativistic corrections are given in the Supporting Information (SI).

To compute the phonon frequencies, We have employed the supercell approach as implemented in the Phonopy[43,44] software, using the VASP code as the force calculator. We also used the VASP code itself to calculate the phonon frequencies with α = 0.6 in *ts*-BVO to confirm the results produced by Phonopy. Both the VASP code and Phonopy use the finite difference to determine the Hessian matrix. In Phonopy, the displacement amplitude is 0.01 Å. In VASP, each ion is subjected to positive and negative displacements of 0.015 Å.

For other materials, the same convergence criteria are imposed as for BVO, as the number of atoms in respective unit cells are the same, and lattice constants of all of the scheelite and fergusonite structures are similar. The pseudopotential of other materials used in all calculations refer to the Materials Project.[45] Briefly, they include Sc ($3s^23p^64s^23d^1$), Lu ($3p^65d^16s^2$), Sm ($5p^66s^24f^3$), Pr ($5p^66s^24f^3$), Y ($4s^24p^65s^24d^1$), La ($5s^25p^66s^25d^1$), Ca ($3s^23p^64s^2$), Nb ($4p^65s^24d^3$), Ta ($5p^66s^25d^3$), and W ($5s^25p^66s^25d^4$).

3. RESULTS AND DISCUSSION

3.1. BVO Calculations Using the PBEsol Functional.

The initial geometries of the primitive cell of *ms*-BVO and *ts*-BVO were taken from experiment[11] and summarized in Table 2. In *ms*-BVO, there are four sets of Bi−O bonds and two sets of V−O bonds. In *ts*-BVO, there are two sets of Bi−O bonds and one set of V−O bonds. Using the plane wave code VASP, we find that after optimization with PBEsol functional, *ts*-BVO remains in the tetragonal phase. The optimized geometry is shown in Figure 2a and reported in Table 2 where it is compared with experiment. Both the lattice parameters and bond lengths of Bi−O and V−O remain close to experimental values. After optimization, we use a 4 × 4 × 4 supercell containing 768 atoms to undertake the phonon calculations of *ts*-BVO. The resulting calculated phonon dispersion with the non-analytical term correction is shown in Figure 2b. We note that there are three real acoustic phonon modes and no soft phonon modes in *ts*-BVO.

Optimization of the *ms*-BVO with the PBEsol functional generates a tetragonal structure as noted above. The structure is shown in Figure 2c and structural parameters are listed in Table 2. The lattice parameters are close to experimental values. But the four sets of Bi−O bond lengths have insignificant differences, and there is only one set of V−O bonds. These values correspond to the tetragonal phase within the error tolerance of $\sim 10^{-3}$ Å. To distinguish it from *ts*-BVO, we denote it *quasi-ts*-BVO. We confirmed this finding using the FHI-aims code which employs atom-centered basis functions. Optimized 4 × 4 × 4 and 6 × 6 × 6 supercells of this *quasi-ts*- BVO structure with 768 and 2592 atoms, respectively, have been used for the phonon calculation with closely matching results. The phonon dispersion with the non-analytical term correction using the 6 × 6 × 6 supercell is shown in Figure 2d, and again there are no soft modes.

Table 2. Lattice Parameters and Bond Lengths of Bi−O and V−O of *ms*-BVO and *ts*-BVO from the Experiment[11] and Optimized with the PBEsol Functional and the Hybrid Functional with α = 0.6 (See Section 2 for Detail)

phases		lattice parameters	Bi−O bond length (Å)	V−O bond length (Å)
ms-BVO	exp.	$\alpha = \beta = 67.911^\circ$	2.676 × 2	1.747 × 2
		$\gamma = 116.403^\circ$	2.533 × 2	1.739 × 2
		$a = b = 6.887$ Å	2.349 × 2	
		$c = 5.215$ Å	2.314 × 2	
	opt.-PBEsol	$\alpha = \beta = 67.979^\circ$	2.457 × 2	1.733 × 4
		$\gamma = 115.951^\circ$	2.456 × 2	
		$a = b = 6.820$ Å	2.420 × 2	
		$c = 5.114$ Å	2.419 × 2	
	opt-hybrid	$\alpha = \beta = 67.934^\circ$	2.601 × 2	1.709 × 2
		$\gamma = 116.450^\circ$	2.477 × 2	1.693 × 2
		$a = b = 6.748$ Å	2.339 × 2	
		$c = 5.127$ Å	2.297 × 2	
ts-BVO	exp.	$\alpha = \beta = 136.195^\circ$	2.450 × 4	1.727 × 4
		$\gamma = 63.680^\circ$	2.494 × 4	
		$a = b = c = 6.899$ Å		
	opt.	$\alpha = \beta = 135.955^\circ$	2.420 × 4	1.733 × 4
		$\gamma = 64.050^\circ$	2.458 × 4	
		$a = b = c = 6.820$ Å		

To test if more modern higher-order methods beyond the capabilities of the PBEsol and PBE functional would yield the required level of accuracy, we also used a Meta-GGA SCAN functional[46] and found that the results are similar to those from the PBEsol functional, which is also confirmed by Laraib et al.[47] Checking the effect of potentially viable local strong correlations, we also tried a DFT + *U* approach with the *U* values on V 3d and O 2p states taken from our previous work.[48] On optimization, however, the monoclinic structure still turned into tetragonal. Furthermore, we also added, in turn, the *U* values of 4, 7, and 10 eV on the Bi 6s state in each case, the structure retained its experimentally observed monoclinic character.

3.2. BVO Calculations with the Hybrid Functional.

Next, we explored the effect of inclusion of a fraction (α ranging from 0 to 1) of the more accurate HF exchange in the DFT expression, that is a hybrid functional.[49] We first optimize *ts*-BVO with the "standard" α = 0.25, then increased the value up to 0.7. *ts*-BVO remains tetragonal after optimization. With α = 0.25, 0.4, and 0.5, there are no soft phonon modes at the Γ point. With α = 0.55 and 0.6, there is a soft optical phonon mode at the Γ point with the values of 0.28*i* and 0.75*i* THz, respectively, that is represented as a negative frequency below the three acoustic modes in Figure 3a. As well as using Phonopy, we also use the finite element method implemented in the VASP code which reports the frequency of the soft mode at the Γ point as 0.87*i* THz with α = 0.6. On inspection of the irreducible representations of the modes, we found that the soft mode has a B_g symmetry. When α = 0.65 and 0.7,

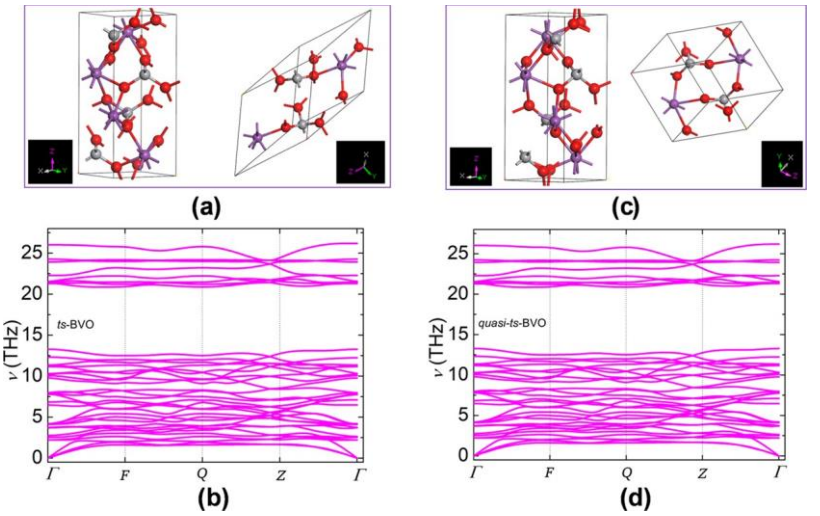

Figure 2. (a) Structure of (right) optimized primitive cell of *ts*-BVO and (left) the common crystallographic unit cell (experimental lattice parameters $a = b = 5.147$, $c = 11.722$ Å) of *ts*-BVO, (b) the phonon dispersion of *ts*-BVO, (c) the structure of (right) the primitive cell of *quasi-ts*-BVO optimized from *ms*-BVO, and (left) the common crystallographic unit cell (experimental lattice parameters $a = 5.215$, $b = 5.084$, $c = 11.706$ Å, $\gamma = 90.394°$) of *ms*-BVO, and (d) the phonon dispersion of *quasi-ts*-BVO. The high symmetry *q*-points are Γ (0, 0, 0), *F* (0, 0.5, 0), *Q* (0, 0.5, 0.5), and *Z* (0.5, 0.5, −0.5), in fractions of the reciprocal lattice vectors. The red spheres, gray spheres, and the purple spheres are O, V, and Bi atoms, respectively.

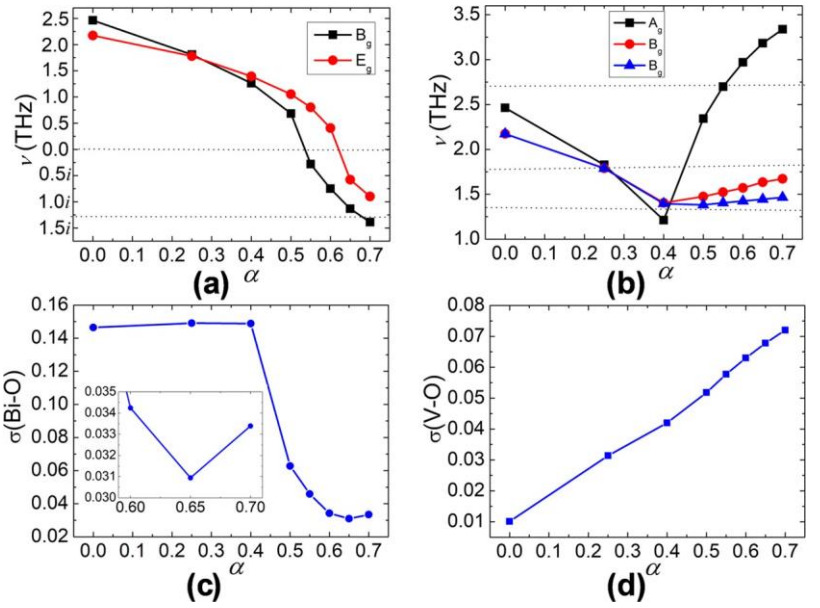

Figure 3. (a) Calculated lowest B_g and E_g frequencies in *ts*-BVO, the dotted line below 0 is the experimental value of the B_g mode at 0 K. (b) The calculated two lowest B_g and one lowest A_g frequencies in *ms*-BVO; the dotted lines are the experimental values at 0 K. (c) Standard deviations of the Bi−O bond length in optimized *ms*-BVO, and (d) standard deviations of the V−O bond length in optimized *ms*-BVO. Experimental phonon mode frequencies are taken from Pinczuk et al.[13] α is the fraction of HF exchange.

there appear three soft optical modes. The lowest soft mode belongs to the B_g representation. The other two modes are degenerate and belong to the E_g representation. The B_g and E_g frequencies in *ts*-BVO for different values of α are shown in Figure 3a.

We next optimized *ms*-BVO with α values of 0.25 (i.e., PBEsol0), 0.4, 0.5, 0.55, 0.6, 0.65, and 0.7. We also performed a calculation with the widely used HSE06 functional (with α = 0.25). We found that when α is less than 0.4, the outcome of the optimization of *ms*-BVO is still *quasi-ts*-BVO. This finding does not seem to be consistent with previous results reported by Kweon et al.[50] based on constant volume calculations where the *ms*-BVO was obtained with the HSE06 (α = 0.25) hybrid functional; however, in our case, we fully relaxed the geometry, including cell dimensions. For values of α from 0.5 to 0.7, the optimization in *ms*-BVO was carried out. We found that an α value of 0.6 gives a monoclinic geometry of *ms*-BVO as shown in Table 1, which is fully consistent with the experimental structure. We also calculated the phonon frequencies using the primitive cell with different values of α. The resulting two lowest B_g and one lowest A_g frequencies in *ms*-BVO are shown in Figure 3b. Moreover, we found with α = 0.7 that there is one soft B_u mode in *ms*-BVO.

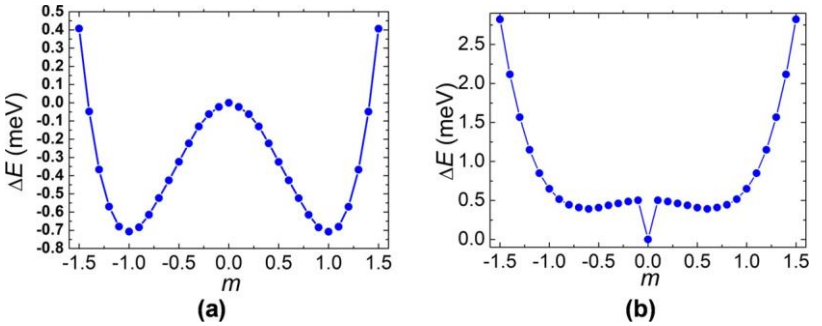

Figure 4. Anharmonic double-well potential along the soft mode at the Γ point with (a) the cut-off energy of 950 eV and (b) the cut-off energy of 650 eV.

To find which value of α is the most appropriate to describe the monoclinic structure, we calculated the standard deviations (SD) of the Bi−O and V−O bond lengths in optimized *ms*-BVO. The SD is defined as $\sigma = \sqrt{\frac{\sum_{i=1}^{n}(x - x_0)^2}{n}}$, where x is the bond length of Bi−O or V−O in optimized *ms*-BVO, and x_0 is the experimental Bi−O or V−O bond length. The σ(Bi−O) and σ(V−O) are shown in Figure 3c,d. The results for σ(Bi−O) show that the calculated structure is close to the experiment for α = 0.65. But the σ(V−O) shows that the smaller the values of α the closer the structure to the experiment. In the displacive transition of BVO, the displacement of Bi plays a key role. So, we consider that σ(Bi−O) is the determining factor here and $\alpha \sim 0.65$ is the most appropriate for modeling *ms*-BVO.

The experimental work of Pinczuk et al.[13] reports one A_g and two B_g modes in *ms*-BVO. With the phase transition from *ms*-BVO to *ts*-BVO, the A_g mode in *ms*-BVO transforms into the B_g mode in *ts*-BVO, and the two B_g modes in *ms*-BVO merge to become the E_g mode in *ts*-BVO. At 0 K, the values of these three modes in *ms*-BVO are shown in Figure 3b. Since the present calculations are athermal, there are no thermal effects nor are zero-point vibrations included. The B_g mode becomes soft in *ts*-BVO with the value from around 1.24*i* to 1.32*i* THz. In our calculations, when α is smaller than 0.5, there is no soft mode in *ts*-BVO. When α = 0.7, there is a soft mode in *ms*-BVO. No experimental data indicate soft modes in *ms*-BVO showing that α should lie between 0.5 and 0.7, and we focus on the values of 0.55, 0.6, and 0.65. With α = 0.65, the E_g mode becomes soft in *ts*-BVO which does not have experimental support. With α = 0.55, the value of the soft B_g frequency in *ts*-BVO is only 0.28*i* THz which is far from the experimental value. From all of these arguments, we recommend α = 0.6 as optimal for describing the phase transition from *ts*-BVO to *ms*-BVO. We have noted that similarcalculations with different conclusions had been reported by Kweon et al.[50] and Laraib et al.[47] Kweon et al.[50] state that the conventional 25% HF admixture to the DFT exchange resultsin excellent agreement with the experiment. They concluded that a lower 10% HF fraction failed to stabilize the monoclinic phase while a higher 50% HF fraction resulted in a significant overestimation of the monoclinic distortion. Their results required constrained relaxations which under careful examina- tion prove to be misleading. Laraib et al.[47] proposed to resolvethis problem by introducing excess electrons in the conductionband of BVO by carrier concentrations (typical of a degenerate semiconductor) are not normally reported for this system.

As described above, we use the fraction of HF exchange α in the hybrid functional as a parameter to "fit" the energy ordering from the experiment and found that large α (∼0.6) works for BVO. We didn't consider the role of entropy or electron−phonon coupling on the system. In fact, neither of these two factors can play a role in stabilizing the low-symmetry phase of BVO, which is simply unstable on the potential energy landscape of GGA,[29] meta-GGA,[46] and common hybrid functionals[41] using low α values. All phonon contributions retain the hard mode nature in the low-symmetry unstable structure and do not make any difference. It is also often proposed that the α values relate more to electronic structure and should be chosen based on the electronically derivedKoopman's conditions[51] (theorem) and dielectric properties;[52] we should point out that this is a matter doping, which however attractive is not convincing as the levels of doping required and resultant

of debate in the literature. This argument has been put forward by a part of the solid-state community; but the choice of α based on these grounds cannot be justified for small molecules for example, and only highlights the problem of non-transferability of α.

Originally, hybrid functionals were introduced in an attempt to reduce the self-interaction error in DFT and improve basic ground-state properties of molecules and solids, which has been successful in many respects where better geometries and binding energies have been obtained for most known compounds only with few notable exceptions. For a wide class of materials, whose valence and conduction states are localized on different chemical components of the system, band gap transitions are charge transfer processes←this is where hybrid DFT with an α value of about 20% has shown a

dramatic improvement in the band gap prediction. This improvement, however, is not observed for many small molecules, where more advanced methods are required foraccurate predictions of one- and two-electron processes (ionization and excitation); such a situation also arises for many solids. In fact, many ground and excited-state propertiesof materials including electron and hole localization, opticaltransitions, activation energies, and rates of diffusion andchemical reactions involving covalent bond breaking orformation, magnetic ordering, etc. are commonly approachedusing differently tuned hybrid functionals, for example, usingthe so-called double exchange Becke's or Minnesota families offunctionals[53] as we have already argued in the above section.Finally, we investigated, in detail, the phase transition between (*quasi*-)*ts*-BVO and *ms*-BVO by modulating thetetragonal structure along the eigenvector of the soft mode

with α = 0.6. We use the formula $X(m) = X(0) + m\triangle X$ to describe the modulated structures, where $X(m)$ is the modulated structure, $X(0)$ is the *ts*-BVO structure, m is the displacement parameter, and $\triangle X$ is the displacement of atoms in the primitive cell along the soft mode at Γ point.

The relative energy ΔE of modulated structures vs m is plotted in Figure 4a. When $m = 0$, it corresponds to *ts*-BVO. As m changes, the structures distort and tend to *ms*-BVO. We found the energy curve of Figure 4a has the form of a classical anharmonic double-well potential, which indicates that the transition between *ts*-BVO and *ms*-BVO is second order in agreement with experiment.[7] The energy barrier for the transition is 0.7 meV*, which indicates that the *ts*-BVO phase may be *effectively* an average structure. We also show in Figure 4b the double-well potentials calculated with a "small" plane wave basis cut-*off* energy of 650 eV. In this case, we determine a lower barrier of ~0.1 meV, but at the highly symmetric m = 0 point, we calculate a spuriously low total energy, which results in the *ts*-BVO phase being more stable than the *ms*-BVO phase. This result is found whether or not we include symmetry constraints in the SCF calculation; thus, the plane wave basis cut-*off* of 650 eV is *insufficient* to describe the phase ordering of BVO, even with α = 0.6. We have tested convergence of the total energy on the primitive cell of the *ms*-BVO with respect to the cut-*off* energy using the PBEsol functional as shown in Figure S1 in the SI. It shows convergence of the cut-*off* energy occuring only around 950 eV.

As with other systems containing heavy elements, spin−orbit coupling (SOC) is important in BVO. We performed several PBEsol calculations including the SOC to investigate the energy ordering and stability of optimized *ms*-BVO and *ts*- BVO structures, including the phonon frequencies at the Γ point of *ts*-BVO, but the results show no *significant difference* from those without SOC. The details of these results are shown in Figures S2 and S3 in the SI.

We also performed calculations including SOC using the PBEsol, PBEsol0, α = 0.4, α = 0.5, and α = 0.6 based on several points on the double-well potential. The results are shown in Figure 5. It is expected that the *ts*-BVO is the lowest energy

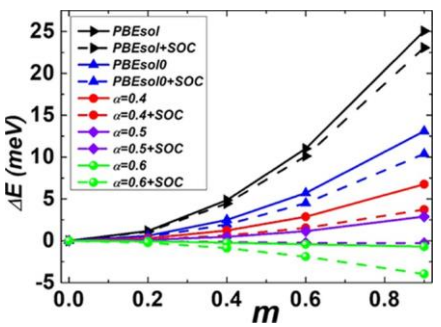

Figure 5. Energy curves of several modulated structures along the soft mode using PBEsol, PBEsol0, α = 0.4, α = 0.5, and α = 0.6 with and without the SOC *effect*. (Solid lines without SOC and dash lines with SOC).

using PBEsol and PBEsol0 even with the SOC corrections. The *ts*-BVO still has the lowest energy using the hybrid functional even with α = 0.4 and 0.5 without SOC. With SOC, for α = 0.4, *ts*-BVO still has the lowest energy. For α = 0.5, the SOC *effect* does stabilize the distorted structure but only slightly. With α = 0.6, the SOC *effect* results in lowered energy and stabilized distorted structure.

3.3. PBEsol and Hybrid Functionals on Other Scheelite-Structured Materials.

In this section, we investigated other selected materials of the scheelite structural family with the PBEsol functional and hybrid functional used in our calculations on BVO that we described above. First, we performed calculations using the PBEsol functional, and the calculated energy *differences* are shown in Table 3. We *find* for

Table 3. Calculated Total Energy and Energy Difference (Per Formula Unit) of Scheelite-Structured ABO_4-Type Materials

materials	E(*ts*-) (eV)	E (*ms*-) (eV)	$\delta[E(ts\text{-})-E(ms\text{-})]$ (eV)
$ScVO_4$	−108.71624916	−108.71738886	0.0011
$LuVO_4$	−107.29007094	−107.28675387	−0.0033
$SmNbO_4$	−110.88526073	−110.95811368	0.0729
$PrNbO_4$	−110.54665351	−110.60848729	0.0618
$YNbO_4$	−110.45240017	−114.85662455	4.4042
$LaNbO_4$	−111.40546747	−111.48119007	0.0757
$YTaO_4$	−120.15048020	−120.34198818	0.1915
$CaWO_4$	−105.43729445	−105.42843104	−0.0089

(Sm, Pr, Y, La) NbO_4 and $YNbO_4$ that the monoclinic structures have lower energy than the tetragonal phase. These materials[17,18,23,35] are similar to BVO, in which the fergusonite monoclinic structures are ferroelastic and low-temperature phase. This indicates that the PBEsol functional can produce the ground state of these structures accurately. For $LuVO_4$ and $CaWO_4$, the scheelite tetragonal phase has lower energy with the PBEsol functional. For these two materials,[14,24] the phase transition from scheelite to fergusonite is induced by high pressure. The scheelite tetragonal phase should be the stable phase, which indicates that the PBEsol functional works well too in these two materials. But for $ScVO_4$, we *find* that the scheelite tetragonal phase and the fergusonite monoclinic phase have almost the same energy using the PBEsol functional indicating that the PBEsol functional cannot distinguish these two phases. Experimental studies indicate that[24,54−56] the low-pressure zircon phase $ScVO_4$ undergoes an irreversible zircon-to-scheelite phase transition above 8.2 GPa. Beyond 18.2 GPa, the scheelite-to-fergusonite phase transition occurs. On the release of pressure, the fergusonite phase was detected down to 11 GPa. Below 11 GPa the sample retains the metastable phase even at ambient pressure. All of these *findings* indicate that the scheelite phase is more stable than the fergusonite phase; however, the scheelite phase may still have a little distortion, which is not observed due to thermal *effects*.

Since the PBEsol functional cannot distinguish the scheelite and the fergusonite phase, we investigated the phase stabilities further using hybrid functional calculations. Based on the unit cell of tetragonal $ScVO_4$, we constructed several monoclinically distorted structures by displacing the two Sc atoms toward (or away) each other with a step of 0.05 Å, then using the monoclinic cell setting optimized all other geometrical parameters using the PBEsol functional. For the resulting optimized structures, we performed single-point calculations using the hybrid functional with α = 0.25 and 0.6. The energy plot as a function of displacement of Sc using *different* functionals is shown in Figure 6. It is obvious that the little distorted scheelite structure becomes more stable with increasing HF exchange.

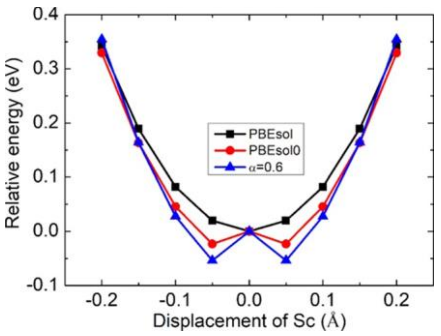

Figure 6. Energy curve with the function of displacement of Sc using different functionals.

3.4. Discussion. In the case of BVO, although we found that functionals with ~60% HF exchange are capable of giving the correct description of the ground state of BVO, they do not give a good description of excited states in the one-electron approximation of the band structure.[50,57] Clearly, calculations of the structure, properties, and lattice dynamics of the compound need high fractions of the exact exchange interaction. The probable reason is the need to accurately describe the Bi 6s lone pair electrons, which are not only needed in phonon calculations as David and Wood[9] argue but are also crucial in determining the geometry of BVO. This point also can be gleaned from the polarizability of the material. We plot the electronic density of states (DOS) calculated with PBEsol, and hybrid functionals using α = 0.25, 0.6, and 0.65 in Figure 7. The fundamental band gap of BVO is

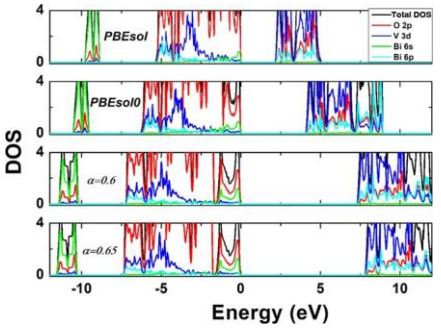

Figure 7. Electronic DOS of *ms*-BVO, the Fermi level is set at the valence band maximum (VBM).

between O 2p and V 3d states. Using PBEsol we calculate this gap to be 2.2 eV, which is close to the experimental value[58] (~2.4 eV), indicating that the PBEsol functional can describe the polarizability of O accurately. The polarizability of Bi in turn will include an on-site contribution from hybridization of its 6s and 6p states, and the charge transfer from Bi 6s to V 3d (mediated by O 2p states). The on-site contribution is notably underestimated with PBEsol (cf. a 13.5 eV calculated gap and experimental value of 15 eV), whereas the charge transfer mechanism, which is determined by a gap of 11.5 eV, is well described.[58] Hybrid functionals, however, gave a much poorer description of these gaps and require at least SOC corrections included in the consideration.[57] These results are in contrast with gas-phase polarizability calculations with the details shown in the Supporting Information. In the gas phase, the polarizability of Bi^{3+} which is shown in Table S1 in the SI is described well with the PBE0 functional while in the BVO material it may be described using the hybrid functional with large fractions of HF exchange.

Furthermore, perhaps, crucially, relative sizes of constituent atoms in BVO play an important role in the phase transition. The V−O bond lengths remain nearly constant, and we find only small standard deviations between the experiment and theory using either PBEsol or hybrid functional calculations, indicating that the sizes of O and V are described with sufficient accuracy. The rigidity of VO_4 tetrahedra in the phase transition has been observed experimentally.[9] For Bi, its position off-center of the BiO_8 dodecahedra plays a key role in the phase transition. The overall stability of *ts*-BVO and the absence of soft modes revealed by PBEsol calculations indicate that the Bi^{3+} ions prove to be too large to move off-center in *ts*-BVO. Standard hybrid functionals like PBEsol0, PBE0, and HSE06 (with α = 0.25) are commonly expected to perform well for average atomic structures and band gaps, but as we found can still fail, as in the present case, when tackling heavy elements, such as Bi. A different weight of the HF exchange is required to reproduce or predict different observables, as a general rule, and, a higher fraction of the HF exchange than 0.25 is required in the solid state, as pointed out by Cora et al..[59] On increasing the HF exchange fraction α from 0 to 0.5, there are still no soft modes in *ts*-BVO meaning that the Bi^{3+} radius is still too large. The effective radii of the Bi^{3+} and O^{2-} ions changing with α are shown in the inserted graph in Figure 8. The effective radii of the Bi^{3+} and O^{2-} ions have been

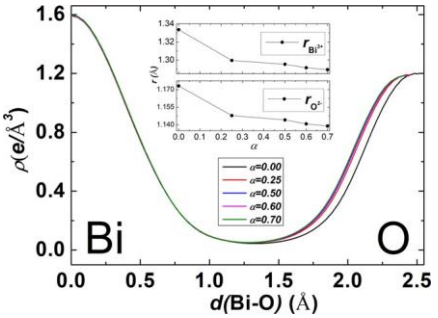

Figure 8. Charge density line profile ρ in unit of e/Å^3 along the longer Bi−O bond in the tetragonal phase of BVO. The graph in the inset is the effective radii of the Bi^{3+} and O^{2-} ions change with α.

obtained from the charge density graphs as distances from the respective nuclei to the density minimum in Figure 8. In the Figure, Bi is on the left and O is on the right. The inset figure clearly shows the ion reduction with α. We have concentrated on the Bi ion in this analysis as the reduction of O is a common effect in all materials of this class, but only BVO proves to be problematic for common DFT approaches. Increasing α further above 0.5, the Bi^{3+} ions become sufficiently small and move readily off-center in the BiO_8 dodecahedra, which explains why we could describe the phase transition in BVO with α = 0.6. This behavior can be attributed to the disbalance in the self-interaction error when describing valence O 2p and Bi 6s lone pair electrons.

4. CONCLUSIONS

A number of popular local, semi-local, and hybrid functionals with low fractions of HF exchange (≤25%) in DFT are widely used and accepted when simulating the properties of materials. Here, we demonstrate, that the basic ground-state structure

and phonon properties of BVO can only be described using a hybrid DFT with an unusually larger fraction of ~60% HF under extremely high convergence criteria. In other scheelite-structured ABO_4 materials, which adopt both scheelite and fergusonite symmetry, we observe a similar behavior with the ground state not reproduced correctly for some of them. In general, based on this work and earlier studies, we find that $LaNbO_4$ are already described well by LDA; $YTaO_4$ and $HoTaO_4$ by PBE; and $HoNbO_4$, $SmNbO_4$, and $SmTaO_4$ by PBEsol. While in BVO and $ScVO_4$, the calculations do require over 50% of HF exchange. Considering recent double hybrid DFT approaches that typically employ high fractions of the HF exchange along with the MP2-type or similar expressions for the nonlocal correlation contributions,[53] we might expect that the problem of finding a unified approach to the whole class of the material lies in the missing nonlocal correlation functional absent in the current generation of popular density functional methods.

Our results not only give a fundamental understanding of the phase transition in BVO but also indicate the challenges, which may face standard DFT or hybrid DFT with only low fractions of HF when investigating the structure and physical properties of materials, especially those with highly polarizable ions. Our findings for BVO are directly relevant for the studies of phase transition in ABO_4-type materials related phase transformations.

ASSOCIATED CONTENT

Supporting Information

The Supporting Information is available free of charge at

Plane wave cut-off energy test; spin−orbit coupling effect on the potential energy landscape of BVO and on the phonon frequencies of *ts*-BVO; details of gas-phase Bi^{3+} polarizability calculations using the NWChem code; and details of FHI-AIMS input (PDF)

AUTHOR INFORMATION

Corresponding Authors

Taifeng Liu − *National & Local Joint Engineering Research Center for Applied Technology of Hybrid Nanomaterials, Henan University, Kaifeng 475004, China; Kathleen Lonsdale Materials Chemistry, Department of Chemistry, University College London, London WC1H 0AJ, United Kingdom;* orcid.org/0000-0002-6869-7022; Email: uccatl0@ucl.ac.uk

Alexey A. Sokol − *Kathleen Lonsdale Materials Chemistry, Department of Chemistry, University College London, London WC1H 0AJ, United Kingdom;* orcid.org/0000-0003-0178-1147; Email: a.sokol@ucl.ac.uk

John Buckeridge − *School of Engineering, London South Bank University, London SE1 OAA, United Kingdom;* orcid.org/0000-0002-2537-5082; Email: j.buckeridge@lsbu.ac.uk

Authors

Xingfan Zhang − *Kathleen Lonsdale Materials Chemistry, Department of Chemistry, University College London, London WC1H 0AJ, United Kingdom;* orcid.org/0000-0003-0852-4194

Jingcheng Guan − *Kathleen Lonsdale Materials Chemistry, Department of Chemistry, University College London, London WC1H 0AJ, United Kingdom*

C. Richard A. Catlow − *Kathleen Lonsdale Materials Chemistry, Department of Chemistry, University College London, London WC1H 0AJ, United Kingdom; School of Chemistry, Cardiff University, Cardiff CF10 1AT, United Kingdom;* orcid.org/0000-0002-1341-1541

Aron Walsh − *Department of Materials, Imperial CollEge London, London SW7 2AZ, United Kingdom;* orcid.org/0000-0001-5460-7033

Author Contributions

All authors contributed to the study reported in this paper. T.L. carried out the calculations and wrote the manuscript; J.B. helped with the calculation details and discussion of the results and edited the manuscript. A.W. provided useful suggestions and made important contributions to the discussion. A.A.S. gave the idea of the work and led the project. C.R.A.C. supervised the project and edited the manuscript. X.Z. performed the NWChem calculations. J.C. provided scripts for eigenvector scanning.

Notes

The authors declare no competing financial interest.

ACKNOWLEDGMENTS

The authors acknowledge funding from EPSRC Grants EP/I01330X/1, EP/K016288/1, and EP/N01572X/1. The authors also acknowledge the use of the UCL Thomas, Faraday, Kathleen, and Grace High Performance Computing Facilities (Thomas@UCL, Faraday@UCL, Kathleen@UCL, and Grace@UCL) and associated support services, and the ARCHER and ARCHER2 supercomputers through the membership of the U.K.'s HPC Materials Chemistry Consortium, which is funded by EPSRC Grants EP/ R029431 and EP/P020194, in the completion of this work.

T.L. acknowledges support from the National Natural Science Foundation of China (grants 21703054 and 22173026) and Henan University's Engineering Research Center for Nanomaterials (ERCN) and International Affairs Office.

ADDITIONAL NOTE

*This barrier size, which is characteristic of many displacive phase transitions, should not be directly compared to the experimental critical temperature; for a realistic comparison, a full investigation of the free-energy landscape with respect to appropriate order parameters would be necessary, which is beyond the scope of the current study.

REFERENCES

(1) Park, Y.; McDonald, K. J.; Choi, K.-S. Progress in Bismuth Vanadate Photoanodes for Use in Solar Water Oxidation. *Chem. Soc. Rev.* 2013, *42*, 2321−2337.

(2) Abdi, F. F.; Berglund, S. P. Recent Developments in Complex Metal Oxide Photoelectrodes. *J. Phys. D: Appl. Phys.* 2017, *50*, No. 193002.

(3) Tayebi, M.; Lee, B.-K. Recent Advances in Bivo4 Semiconductor Materials for Hydrogen Production Using PhotoelectrochemicalWater Splitting. *Renewable Sustainable Energy Rev.* 2019, *111*, 332− 343.

(4) Wang, Z.; Huang, X.; Wang, X. Recent Progresses in the Design of $BiVO_4$-Based Photocatalysts for Efficient Solar Water Splitting. *Catal. Today* 2019, *335*, 31−38.
(5) Kudo, A.; Omori, K.; Kato, H. A. Novel Aqueous Process for Preparation of Crystal Form-Controlled and Highly Crystalline $BiVO_4$ Powder from Layered Vanadates at Room Temperature and Its Photocatalytic and Photophysical Properties. *J. Am. Chem. Soc.* 1999, *121*, 11459−11467.
(6) Li, R.; Zhang, F.; Wang, D.; Yang, J.; Li, M.; Zhu, J.; Zhou, X.; Han, H.; Li, C. Spatial Separation of Photogenerated Electrons and Holes among {010} and {110} Crystal Facets of $BiVO_4$. *Nat. Commun.* 2013, *4*, No. 1432.
(7) Bierlein, J. D.; Sleight, A. W. Ferroelasticity in $BiVO_4$. *Solid State Commun.* 1975, *16*, 69−70.
(8) David, W. I. F.; Glazer, A. M.; Hewat, A. W. The Structure and Ferroelastic Phase Transition of $BiVO_4$. *Phase Transitions* 1979, *1*, 155−169.
(9) David, W. I. F.; Wood, I. G. Ferroelastic Phase Transition in $BiVO_4$: V. Temperature Dependence of Bi^{3+} Displacement and Spontaneous Strains. *J. Phys. C: Solid State Phys.* 1983, *16*, 5127−5148.
(10) David, W. I. F.; Wood, I. G. Ferroelastic Phase Transition in $BiVO_4$: Vi. Some Comments on the Relationship between Spontaneous Deformation and Domain Walls in Ferroelastics. *J. Phys. C: Solid State Phys.* 1983, *16*, 5149−5166.
(11) Sleight, A. W.; Chen, H.-y.; Ferretti, A.; Cox, D. E. Crystal Growth and Structure of $BiVO_4$. *Mater. Res. Bull.* 1979, *14*, 1571−1581.
(12) Pinczuk, A.; Welber, B.; Dacol, F. Mechanism of the Ferroelastic Transition of $BiVO_4$. *Solid State Commun.* 1979, *29*, 515−518.
(13) Pinczuk, A.; Burns, G.; Dacol, F. Soft Optical Phonon in Ferroelastic $BiVO_4$. *Solid State Commun.* 1977, *24*, 163−165.
(14) Errandonea, D.; Manjón, F. J. On the Ferroelastic Nature of the Scheelite-to-Fergusonite Phase Transition in Orthotungstates and Orthomolybdates. *Mater. Res. Bull.* 2009, *44*, 807−811.
(15) Errandonea, D.; Manjón, F. J. Pressure Effects on the Structural and Electronic Properties of ABX_4 Scintillating Crystals. *Prog. Mater. Sci.* 2008, *53*, 711−773.
(16) Popolitov, V. I.; Ivanova, L.; Stephanovitch, S. Y.; Chetchkin, V.; Lobachev, A.; Venevtsev, Y. N. Ferroelectrics ABO4: Synthesis of Single Crystals and Ceramics; Dielectric and Nonlinear Optical Properties. *Ferroelectrics* 1974, *8*, 519−520.
(17) Nikiforova, G. E.; Khoroshilov, A. V.; Gavrichev, K. S.; Knyazev, A. V.; Knyazeva, S. S. Fergusonite−Scheelite Phase Transition of Praseodymium Orthoniobate. *Inorg. Mater.* 2019, *55*, 964−967.
(18) Huse, M.; Skilbred, A. W. B.; Karlsson, M.; Eriksson, S. G.; Norby, T.; Haugsrud, R.; Knee, C. S. Neutron Diffraction Study of the Monoclinic to Tetragonal Structural Transition in $LaNbO_4$ and Its Relation to Proton Mobility. *J. Solid State Chem.* 2012, *187*, 27−34.
(19) Fjeld, H.; Toyoura, K.; Haugsrud, R.; Norby, T. Proton Mobility through a Second Order Phase Transition: Theoretical and Experimental Study of $LaNbO_4$. *Phys. Chem. Chem. Phys.* 2010, *12*, 10313−10319.
(20) Arulnesan, S. W.; Kayser, P.; Kimpton, J. A.; Kennedy, B. J. Studies of the Fergusonite to Scheelite Phase Transition in $LnNbO_4$ Orthoniobates. *J. Solid State Chem.* 2019, *277*, 229−239.
(21) Auckett, J. E.; Lopez-Odriozola, L.; Clark, S. J.; Evans, I. R. Exploring the Nature of the Fergusonite−Scheelite Phase Transition and Ionic Conductivity Enhancement by Mo^{6+} Doping in $LaNbO_4$. *J. Mater. Chem. A* 2021, *9*, 4091−4102.
(22) Aldred, A. T. Cell Volumes of APO_4, AVO_4, and $ANbO_4$ Compounds, Where a= Sc, Y, La−Lu. *Acta Crystallogr., Sect. B: Struct. Sci.* 1984, *40*, 569−574.
(23) Sarin, P.; Hughes, R. W.; Lowry, D. R.; Apostolov, Z. D.; Kriven, W. M. High-Temperature Properties and Ferroelastic Phase Transitions in Rare-Earth Niobates ($LnNbO_4$). *J. Am. Ceram. Soc.* 2014, *97*, 3307−3319.
(24) López-Solano, J.; Rodríguez-Hernández, P.; Muñoz, A. Ab Initio Study of High-Pressure Structural Properties of the Luvo4 and $ScVO_4$ Zircon-Type Orthovanadates. *High Pressure Res.* 2009, *29*, 582−586.
(25) Kondrat'eva, O. N.; Nikiforova, G. E.; Tyurin, A. V.; Ryumin, M.; Gurevich, V.; Kritskaya, A.; Gavrichev, K. Calorimetric Study of Ytterbium Orthovanadate $YbVO_4$ Polycrystalline Ceramics. *Ceram. Int.* 2018, *44*, 18103−18107.
(26) Errandonea, D.; Lacomba-Perales, R.; Ruiz-Fuertes, J.; SEgura, A.; Achary, S. N.; Tyagi, A. K. High-Pressure Structural Investigation of Several Zircon-Type Orthovanadates. *Phys. Rev. B* 2009, *79*, No. 184104.
(27) Feng, J.; Shian, S.; Xiao, B.; Clarke, D. R. First-Principles Calculations of the High-Temperature Phase Transformation in Yttrium Tantalate. *Phys. Rev. B* 2014, *90*, No. 094102.
(28) Levin, I., Nist Inorganic Crystal Structure Database (Icsd); National Institute of Standards and Technology, 2018.
(29) Perdew, J. P.; Burke, K.; Ernzerhof, M. Generalized Gradient Approximation Made Simple. *Phys. Rev. Lett.* 1996, *77*, 3865−3868.
(30) Blokhin, E.; Gryaznov, D.; Kotomin, E.; Evarestov, R.; Maier, J. A Comparative Hybrid DFT Study of Phonons in Several $SrTiO_3$ Phases. *IntEgr. Ferroelectr.* 2011, *123*, 18−25.
(31) Xie, Y.; Yu, H.-t.; Zhang, G.-x.; Fu, H.-g. Lattice Dynamics Investigation of Different Transition Behaviors of Cubic $BaTiO_3$ and $SrTiO_3$ by First-Principles Calculations. *J. Phys.: Condens. Matter* 2008, *20*, No. 215215.
(32) Heifets, E.; Kotomin, E.; Trepakov, V. A. Calculations for Antiferrodistortive Phase of $SrTiO_3$ perovskite: Hybrid Density Functional Study. *J. Phys.: Condens. Matter* 2006, *18*, 4845−4851.
(33) Zhang, Q.; Cagin, T.; Goddard, W. A. The Ferroelectric and Cubic Phases in $BaTiO_3$ Ferroelectrics Are Also Antiferroelectric. *Proc. Natl. Acad. Sci. U.S.A.* 2006, *103*, 14695−14700.
(34) Chen, Z.-X.; Chen, Y.; Jiang, Y.-S. Dft Study on Ferroelectricity of $BaTiO_3$. *J. Phys. Chem. B* 2001, *105*, 5766−5771.
(35) Mullens, B. G.; Avdeev, M.; Brand, H. E. A.; Mondal, S.; Vaitheeswaran, G.; Kennedy, B. J. Insights into the Structural Variations in $SmNb_{1-x}Ta_xO_4$ and $HoNb_{1-x}Ta_xO_4$ Combined Experimental and Computational Studies. *Dalton Trans.* 2021, *50*, 9103−9117.
(36) Csonka, G. I.; Perdew, J. P.; Ruzsinszky, A.; Philipsen, P. H.; Lebègue, S.; Paier, J.; Vydrov, O. A.; Ángyán, J. G. Assessing the Performance of Recent Density Functionals for Bulk Solids. *Phys. Rev. B* 2009, *79*, No. 155107.
(37) Kuwabara, A.; Haugsrud, R.; Stølen, S.; Norby, T. Local Condensation around Oxygen Vacancies in T-$LaNbO_4$ from First Principles Calculations. *Phys. Chem. Chem. Phys.* 2009, *11*, 5550−5553.
(38) Evarestov, R. A.; Bandura, A. V. First-Principles Calculations on the Four Phases of $BaTiO_3$. *J. Comput. Chem.* 2012, *33*, 1123−1130.
(39) Kresse, G.; Furthmüller, J. Efficient Iterative Schemes for Ab Initio Total-Energy Calculations Using a Plane-Wave Basis Set. *Phys. Rev. B* 1996, *54*, 11169−11186.
(40) Kresse, G.; Furthmüller, J. Efficiency of Ab-Initio Total Energy Calculations for Metals and Semiconductors Using a Plane-Wave Basis Set. *Comput. Mater. Sci.* 1996, *6*, 15−50.
(41) Adamo, C.; Barone, V. Toward Reliable Density Functional Methods without Adjustable Parameters: The PBE0 Model. *J. Chem. Phys.* 1999, *110*, 6158−6170.
(42) Blum, V.; Gehrke, R.; Hanke, F.; Havu, P.; Havu, V.; Ren, X.; Reuter, K.; Scheffler, M. Ab Initio Molecular Simulations with Numeric Atom-Centered Orbitals. *Comput. Phys. Commun.* 2009, *180*, 2175−2196.
(43) Togo, A.; Oba, F.; Tanaka, I. First-Principles Calculations of the Ferroelastic Transition between Rutile-Type and $CaCl_2$-Type SiO_2 at High Pressures. *Phys. Rev. B* 2008, *78*, No. 134106.
(44) Togo, A.; Tanaka, I. First Principles Phonon Calculations in Materials Science. *Scr. Mater.* 2015, *108*, 1−5.

(45) Jain, A.; Ong, S. P.; Hautier, G.; et al. Commentary: The Materials Project: A Materials Genome Approach to Accelerating Materials Innovation. *APL Mater.* 2013, *1*, No. 011002.
(46) Sun, J.; Remsing, R. C.; Zhang, Y.; Sun, Z.; Ruzsinszky, A.; Peng, H.; Yang, Z.; Paul, A.; Waghmare, U.; Wu, X.; et al. Accurate First-Principles Structures and Energies of Diversely Bonded Systems from an Efficient Density Functional. *Nat. Chem.* 2016, *8*, 831−836.
(47) Laraib, I.; Carneiro, M. A.; Janotti, A. Effects of Doping on the Crystal Structure of $BiVO_4$. *J. Phys. Chem. C* 2019, *123*, 26752−26757.
(48) Liu, T.; Zhao, Q.; Li, C.; Lyu, Y.; Dupuis, M. Photocatalytic Facet Selectivity in $BiVO_4$ Nanoparticles: Polaron Electronic Structure and Thermodynamic Stability Considerations for Photocatalysis. *J. Phys. Chem. C* 2019, *123*, 20142−20151.
(49) Becke, A. D. A. New Mixing of Hartree−Fock and Local Density-Functional Theories. *J. Chem. Phys.* 1993, *98*, 1372−1377.
(50) Kweon, K. E.; Hwang, G. S. Hybrid Density Functional Study of the Structural, Bonding, and Electronic Properties of Bismuth Vanadate. *Phys. Rev. B* 2012, *86*, No. 165209.
(51) Koopmans, T. Über Die Zuordnung Von Wellenfunktionen Und Eigenwerten Zu Den Einzelnen Elektronen Eines Atoms. *Physica* 1934, *1*, 104−113.
(52) Wang, W.; Strohbeen, P. J.; Lee, D.; Zhou, C.; Kawasaki, J. K.; Choi, K.-S.; Liu, M.; Galli, G. The Role of Surface Oxygen Vacancies in $BiVO_4$. *Chem. Mater.* 2020, *32*, 2899−2909.
(53) Stein, F.; Hutter, J.; Rybkin, V. V. Double-Hybrid Dft Functionals for the Condensed Phase: Gaussian and Plane Waves Implementation and Evaluation. *Molecules* 2020, *25*, No. 5174.
(54) Panchal, V.; Manjón, F. J.; Errandonea, D.; Rodriguez-Hernandez, P.; López-Solano, J.; Muñoz, A.; Achary, S. N.; Tyagi, A. K. High-Pressure Study of $ScVO_4$ by Raman Scattering and Ab Initio Calculations. *Phys. Rev. B* 2011, *83*, No. 064111.
(55) Garg, A. B.; Errandonea, D.; Rodríguez-Hernández, P.; Muñoz, A. Scvo4under Non-Hydrostatic Compression: A New Metastable Polymorph. *J. Phys.: Condens. Matter* 2017, *29*, No. 055401.
(56) Sheng, S.-F. Pressure-Induced Phase Transition for $ScVO_4$: A First-Principles Study. *Phys. B* 2013, *426*, 20−23.
(57) Wiktor, J.; Reshetnyak, I.; Ambrosio, F.; Pasquarello, A. Comprehensive Modeling of the Band Gap and Absorption Spectrum of $BiVO_4$. *Phys. Rev. Mater.* 2017, *1*, No. 022401.
(58) Cooper, J. K.; Gul, S.; Toma, F. M.; Chen, L.; Glans, P.-A.; Guo, J.; Ager, J. W.; Yano, J.; Sharp, I. D. Electronic Structure of Monoclinic $BiVO_4$. *Chem. Mater.* 2014, *26*, 5365−5373.
(59) Cora, F.; Alfredsson, M.; Mallia, G.; Middlemiss, D. S.; Mackrodt, W. C.; Dovesi, R.; Orlando, R. The Performance of Hybrid Density Functionals in Solid State Chemistry. In *Principles and Applications of Density Functional Theory in Inorganic Chemistry*,II Kaltsoyannis, N.; McGrady, J. E., Eds.; Springer Berlin Heidelberg: Berlin, Heidelberg, 2004; pp 171−232.